Engineered Science
DOI: https://dx.doi.org/10.30919/es1337

Structural Numerical Simulations on Shape Memory Alloys Based Actuators

M. Battaglia,[1,*] A. Sellitto,[1] V. Acanfora,[1] M. Zarrelli[2] and A. Riccio[1]

Abstract

This research represents a significant advance in the application of shape memory alloy (SMA) materials in engineering applications, mainly in the field of actuators. The study proposes a comprehensive study of the thermomechanical behavior of SMA materials and implements their peculiar properties by implementing a user material subroutine (UMAT). The UMAT demonstrates high predictive accuracy and has been validated in simulating the behavior of SMA spring within the complex system of an actuator. This verification provides the framework for the design of customized components, as demonstrated by the bistable actuator, proposing alternative solutions for improving the efficiency of this type of actuator compared to its traditional counterparts. Furthermore, the paper includes numerical analyses of a patented bistable actuator, providing justifications for its geometric characteristics. The integration of additive technology and advanced materials addresses the challenges of temperature considerations, leading to innovative solutions. The actuator's stability, responsiveness to various electrical loads, and practical applicability underline the success of combining these cutting-edge technologies.

Keywords: Bistable actuator; Shape memory alloys; Shape memory alloys (SMA) actuator; Finite element method (FEM).
Received: 20 May 2024; Revised: 02 December 2024; Accepted: 04 December 2024.
Article type: Research article.

1. Introduction

Shape memory alloys (SMAs) have gained significant interest in the scientific and engineering communities due to their potential to address a variety of scientific and technological challenges. These metallic alloys, characterized by unique properties such as excellent damping capacity,[1,2] fatigue resistance,[3] and corrosion resistance,[4] find applications across different sectors. In the biomedical field, SMAs have been widely used for several years in orthodontic and orthopedic applications, as mentioned in Ref. [5]. In the automotive sector, some applications and challenges of SMA utilization are described in Ref. [6]. Over the last two decades, numerous applications of SMAs in the aerospace industry have been studied, designed, modeled, and tested.[7] Specifically, the authors in Refs. [8,9] reported some applications, such as the experimental validation of the F-15 inlet using the NASA Langley wind tunnel and the use of SMA elements as actuators for variable geometry chevrons.

[1] *Department of Engineering, University of Campania "Luigi Vanvitelli", via Roma 29, Aversa, CE, 81031, Italy*
[2] *National Research Council of Italy (CNR), Institute for Polymers, Composite and Biomaterials (IPCB), Portici, 80055, Italy*
**Email:* miriam.battaglia@unicampania.it (M. Battaglia)

The distinctive mechanical and thermal properties of SMAs and their ability to maintain a predefined shape and alter it through the application of thermal loads make them particularly suitable for cutting-edge and innovative applications.[10,11] At the basis of the SMA theory lies the reversible microscopic transition between the martensitic and austenitic phases.[12] The volumetric fraction of martensite in SMAs plays an important role, significantly influencing the behavior and performance of these innovative materials.[13] This parameter, representing the volume occupied by the martensitic phase relative to the total material volume, is a key parameter in shaping the thermomechanical response of SMAs.[14] It directly impacts the ability of these alloys to generate significant deformations during loading and unloading cycles,[15] providing the basis for their utilization as high-performance actuators. Accurate understanding and manipulation of the volumetric fraction of martensite are essential for optimizing SMA performance in various phenomena, such as buckling or enhancing performance in low-velocity impact scenarios.[16,17] A thorough analysis of this parameter allows for addressing challenges such as thermomechanical hysteresis,[18] guiding the design of new materials and devices that leverage the unique properties of SMAs.

The ability to assume two stable equilibrium states

introduces some innovative solutions in actuator design, offering a wide range of possibilities for creating adaptable and efficient devices. The use of SMAs as fundamental elements in actuator design for various applications[19,20] proves highly efficient, thanks to their biocompatibility, compact dimensions, and the ability to operate silently, factors that enhance their versatility.[20,21] Indeed, SMA actuators offer many advantages when designed with appropriate criteria.[22] The demand for low activation voltages not only makes them energy-efficient but also opens the door to sustainable and low-energy solutions, proving crucial in an era of innovation and sustainability. However, the implementation of SMA actuators is not without challenges. Managing material fatigue in repeated cycles emerges as a crucial consideration,[23] necessitating innovative approaches to ensure the system's durability and reliability over time.

Moreover, the opportunities for shape memory alloys can be further exploited in conjunction with the potentialities of additive manufacturing (AM), which is a fascinating and multidisciplinary research field. AM represents a significant innovation in the field of industrial production and prototyping.[24,25] The ability to build objects layer by layer from digital data has introduced new paradigms in the design and manufacture of complex components. Among the main benefits of this emerging technology is the freedom of design, allowing the creation of complex and optimized geometries otherwise impossible to achieve with traditional methods.[26,27] This versatility has significant implications in the aerospace,[28] medical,[29] and automotive industries,[30] where lightness and structural complexity can be decisive. In addition, AM offers the possibility of production on demand, reducing material waste and reducing costs related to mass production processes. Large-scale customization becomes a reality, with the ability to adapt each component to the specific needs of the application. This "just-in-time" approach not only improves efficiency, but also has the potential to revolutionize supply chain logistics.[31] Despite the promise of a new era of flexibility and innovation, AM faces significant challenges. Managing the mechanical and thermal properties of printed materials is essential, as production processes can have a substantial impact on final performance.[32,33] This challenge becomes particularly relevant in the context of shape memory alloys, where precision and consistency of material properties are of critical importance. The connection between the potentialities of AM and the specific needs of shape memory alloys is an interesting and multidisciplinary research ground. This research aims to address several engineering needs that require compact size, high actuation forces, fast response, and efficiency in terms of direct current. Indeed, SMA actuators reported in the literature do not meet all these requirements, for instance, in Refs. [34, 35], there is a need for direct current, which makes them inefficient. While actuators with dimensions similar to the one in this study are presented, they ensure very low forces in Refs. [36,37]. Moreover, this study introduces an innovative approach that integrates numerical predictions, additive AM, and experimental validation to investigate SMAs for engineering applications. The approach emphasizes precise design methodologies and detailed numerical analysis to achieve comprehensive insights into SMA behavior. The main objective is to clarify a comprehensive understanding of the thermomechanical behavior of SMAs. The decision to base the work on the numerical implementation of the thermomechanical behavior of SMAs reflects the need to validate the proposed model. This approach allows for a thorough and reliable understanding of the complex responses exhibited by SMAs. The validation of the proposed model has been conducted through an integrated approach, which combines in-depth numerical analyses with experimental literature tests. After the validation of the numerical model, a numerical analysis has been performed on a patented bistable actuator fabricated using additive manufacturing (AM) technology. Its geometrical characteristics and force outputs have been confirmed subsequently. AM plays a crucial role in this process, allowing a significant weight reduction of around 40% and offering the possibility of selecting materials that can withstand the required high temperatures. Furthermore, experimental actuation tests have been conducted to assess the system's response time. The combination of a valid numerical model and the application of AM to produce bistable actuators represents an innovative approach that could open new horizons in the potential applications of shape memory alloys, thus contributing to the advancement of research and the development of practical solutions in various technological fields.

In section 2, the SMA constitutive model is presented. The validation of the user material subrotuine (UMAT) and numerical results of the patented bistable actuator are detailed in section 3. In section 4, the additive configuration and experimental test are described. Conclusions are reported in section 5.

2. Theoretical background: SMA constitutive model

Since the 1980s, extensive research has been conducted in the field of constitutive modeling for SMAs, aiming to elucidate the primary models governing their behavior. These resultant models can be broadly categorized into micro, micro-macro, or macro classifications.

Micro models are specifically designed to unravel intricate micro-scale features such as nucleation, interface motion, twin growth, and more. Micro-macro studies represent a fusion of micromechanics with macroscopic continuum mechanics, striving to formulate constitutive laws for SMAs. On the contrary, phenomenological or macro approaches leverage macroscopic variables to articulate the average behavior of SMA materials. Well-suited for integration into numerical methods like the finite element method, these macro models efficiently forecast the effective behavior of SMA components and devices.

This research presents the numerical implementation of the

behavior of shape memory alloys subjected to tension or temperature loads, employing the Brinson model to define the specific characteristics of these alloys.[38] A subroutine in the Abaqus software has been specifically designed to replicate the experimental behavior of shape memory materials under mechanical and thermal stresses in a numerical environment. The implemented model considers internal variables describing the material's internal structure, with these variables and control variables such as mechanical strain, temperature, Young's modulus change, and volumetric fraction of martensite defined as state variables. This model falls under the classification of assumed phase transformation kinetics, where the volumetric fraction of martensite is an internal variable governing various phase transitions. In the context of this research, the accurate implementation of a material model is important to address critical issues associated with shape memory alloys, ensuring a faithful replication of real-world behavior and enabling comprehensive design in a numerical environment.

The foundation of shape memory alloys lies in their different crystal structure exhibited under specific conditions, leading to distinct phases known as austenite and martensite. Austenite possesses a BCC structure, whereas martensite has a more flexible, distorted structure. The transition between these phases results in the two primary effects of shape memory alloys: the pseudo-elastic effect (PE) and the shape memory effect (SME). The combination of these two effects makes this type of alloy particularly suitable for engineering applications.

According to the phase diagram proposed by Brinson, a numerical approach has been formulated to reproduce the thermomechanical behavior (Fig. 1).

The phase diagram depicted in Fig. 1 is an important tool for comprehending and predicting the behaviour of an SMA across different temperature and stress conditions. This diagram delineates the various phases in which SMAs can exist at different temperature and stress levels. Distinct regions within the diagram denote different states of the material. In Region 1, a combination of high stress and low temperature leads to the presence of detwinned Martensite phase. Region 2 encompasses twinned Martensite, formed during cooling below the martensite start temperature (*Ms*) under stress-free conditions. In the intermediate region 3, the alloy can coexist in both Austenite and Martensite phases. Conversely, region 4, characterized by high temperature and low stress, signifies the presence of the alloy in the Austenite phase.

The phase diagram establishes key parameters such as C_{AM}^{*} and C_{MA}^{*}, representing the band slope for forward and reverse phase transformations in the (σ, T) diagram. Additionally, σ_{scr} and σ_{fcr} denote the critical stress values for the start and end of the austenite-to-martensite phase transformation. The thermomechanical properties of the alloys are scrutinized based on the outlined diagram, showcasing the alloy's varied response contingent on its initial temperature state before undergoing mechanical or thermal deformation.

The austenite end temperature (A_f) is a key parameter in characterizing the behavior of SMAs. The importance of the A_f temperature lies in its direct influence on the performance and applications of SMAs. At high temperatures ($T \geq A_f$), the application of stress induces a phase transition from Austenite to Martensite. Conversely, removing stress prompts the reverse transition from Martensite to Austenite, culminating in no residual strain, as depicted in the stress-strain diagram in Fig. 2(a).

Figure 2(b) demonstrates the manifestation of the shape memory effect. In the loading and unloading phases at low-temperature conditions ($T \leq A_f$), noticeable residual deformation is observed in the shape memory alloy, and this deformation can be subsequently recovered through the application of thermal loading.

The volume fraction of martensite (ξ) is one of the main parameters in shape memory alloys. Therefore, holds an essential role in determining the mechanical and thermal properties of these materials. The importance of the volume fraction of martensite lies in its direct relationship to the deformation and recovery properties of the alloy. Specifically, the amount of martensite present affects the material's ability to return to its original shape after being thermally or mechanically deformed. Therefore, accurate management of the volume fraction of martensite is essential to optimize the performance and reversibility of shape memory alloys in practical applications. The model used for the analysis closely resembles the constitutive equation framework outlined in the Tanaka model.[39] However, it introduces a distinct approach to phase kinetics by employing a cosine function to represent the martensite volume fraction in relation to both stress and temperature.[40] An example of volume fraction variation as a function of temperature is shown in Fig. 3a.

A mathematical expression that describes this behaviour can be found in a cosine function (Fig. 3), which illustrates the four key temperatures associated with the martensitic transformation: martensite finish transformation stress (M_f), martensite start transformation stress (M_s), austenite start transformation stress (A_s), and austenite finish transformation stress (A_f). To analyse this function, it is necessary to shift the abscissa up to the dotted line from the continuous line to achieve a value of $\xi = 0$ at $T = \pi$. Fit a cosine function in such a way that the function takes on values of $\xi = 1$ at θ=θ and $\xi = 0$ at $\theta = \pi$. The transformation from austenite to martensite can be written as follows:

$$\xi = C_1 \cos \alpha_M \, (T - M_f) + \, C_2 = C_1 \cos \theta + C_2 \quad (1)$$

$$\xi = 0 \text{ at } \theta = \pi \Rightarrow C_1 = C_2 \quad (2)$$

$$\xi = 1 \text{ at } \theta = 0 \Rightarrow C_1 = C_2 = 1 \quad (3)$$

Thus, the transformation from austenite to martensite ($A \rightarrow M$)may is represented as:

$$\xi = \frac{1}{2} \cos \alpha_M \, (T - M_f) + \, 1 \quad (4)$$

As $\xi = 0$ at $\theta = \alpha_M \left(T - M_f\right) = \pi$,

$$\alpha_M = \frac{\pi}{M_s - M_f}, \; M_f \leq T \leq M_s \quad (5)$$

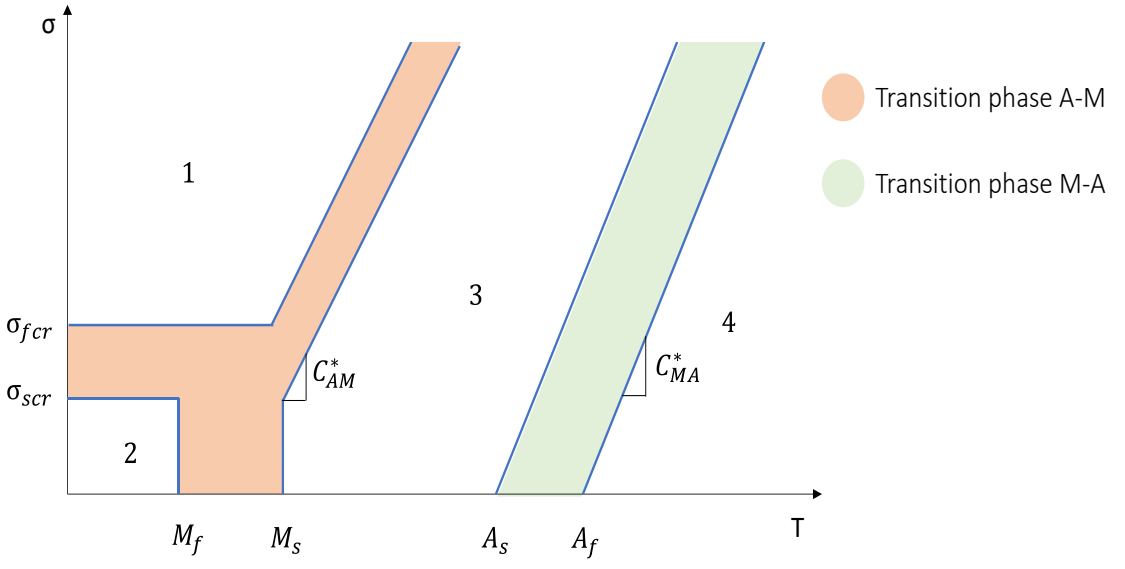

Fig. 1 Phase diagram of a shape memory alloy (σ-T diagram phase).[38]

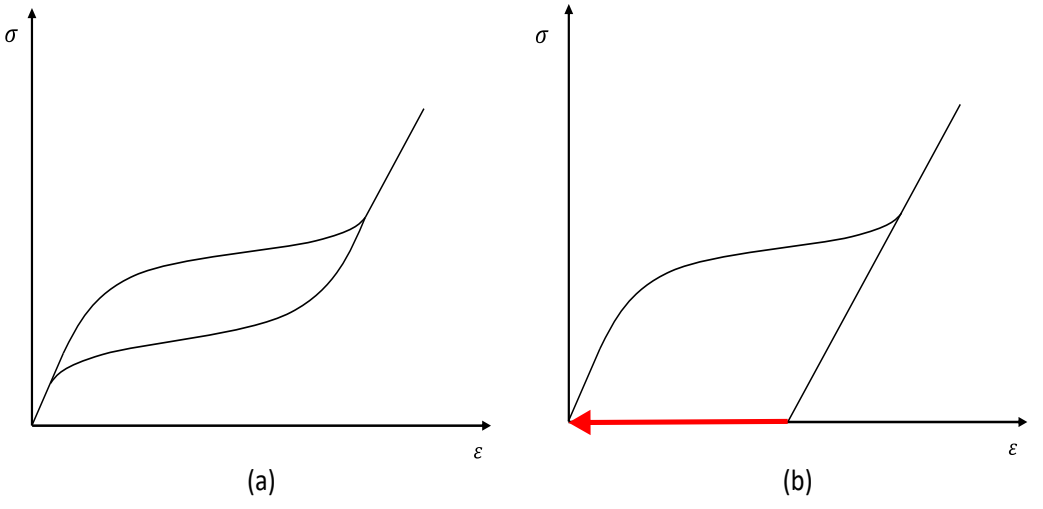

Fig. 2 (a) Pseudo-elastic behavior; (b) Shape memory effect.

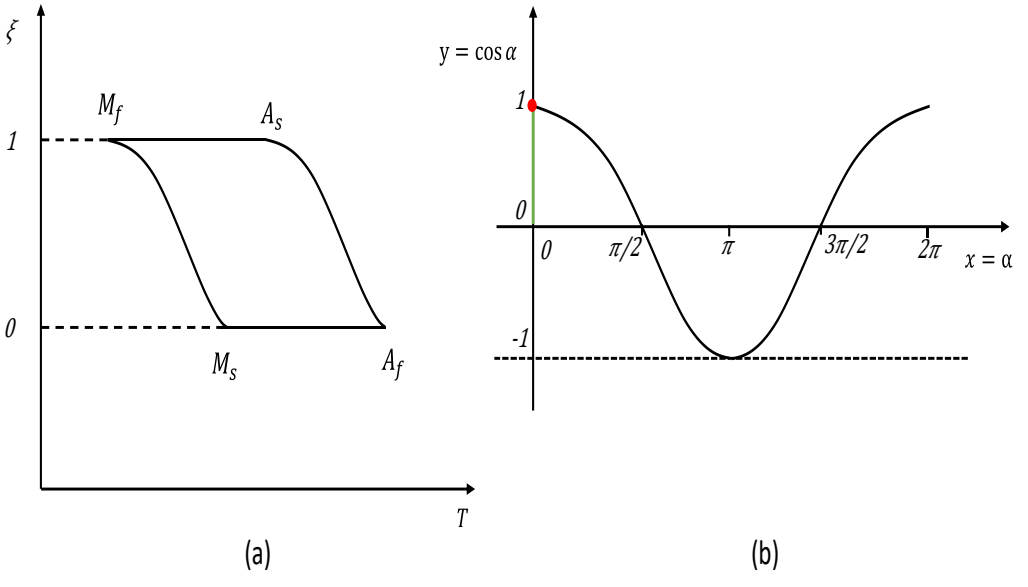

Fig. 3 (a) Volumetric Martensite Fraction at Critical Temperature; (b) cosine function.

Similarly, the order end of the graphical representation ($M \rightarrow A$) can be written as:

$$\xi = \frac{1}{2}\cos\alpha_A\,(T - A_s) + 1 \quad (6)$$

where

$$\alpha_A = \frac{\pi}{A_f - A_s},\ A_s \le T \le A_f \quad (7)$$

However, if the process begins at some value ξ_0 at a corresponding T_0, the above expressions can be modified as follows. The equations are obtained on the basis that no new martensite is added until the temperature T reaches M_s.

Application of the boundary conditions $\xi = 1$ at $\theta = 0$ and $\xi = \xi_0$ at $\theta = \pi$ to (1) leads to the constants:

$$C_1 = \frac{1-\xi_0}{2} \quad (8)$$

$$C_2 = \frac{1+\xi_0}{2} \quad (9)$$

Therefore,

$$\xi = \frac{1-\xi_0}{2}\cos\alpha_M\,(T - M_f) + \frac{1+\xi_0}{2} \quad (A \rightarrow M) \quad (10)$$

For the transformation from $A \rightarrow M$ beginning with $\xi = \xi_0$ and $T = 0$ based on the assumption that no new austenite is added until the temperature reaches A_s, it is possible to write.

$$\xi = 0 \text{ at } \theta = \pi \Rightarrow C_1 = C_2 \quad (11)$$

$$\xi = \xi_0 \text{ at } \theta = 0 \Rightarrow C_1 = \frac{\xi_0}{2} = C_2 \quad (12)$$

$$\xi = \xi_0 \cos[2\,\alpha_A\,(T - A_s)] + 1 \quad (13)$$

2.1 Influence of stress on the characteristic temperatures

Experimental observations indicate that the characteristic temperatures M_s, M_f, A_s, and A_f increase with stress (Fig. 4).

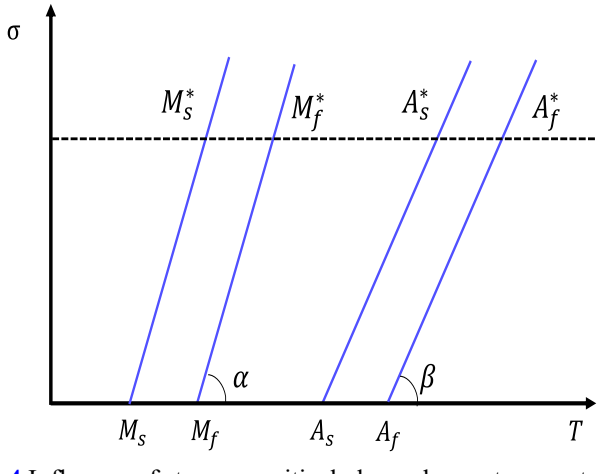

Fig. 4 Influence of stress on critical phase change temperatures.

These changes are described by the slopes C_M and C_A.

$$C_M = \tan\alpha \quad (14)$$

$$C_A = \tan\beta \quad (15)$$

Generally, it is assumed that $\alpha = \beta$ and M_s, M_f, A_s, and A_f are the critical temperatures at which phase occurs at $\sigma = 0$. With $\sigma \neq 0$, higher temperatures will be needed to bring about a phase change. This increase is linear, with critical temperatures increasing with applied stress.

For $(A \rightarrow M)$ transformation with $\sigma \neq 0$,

$$\xi = 1\cos[2\alpha_A(T - A_s) + b_A\sigma] + 1 \quad (16)$$

This equation reflects an increase in temperature proportional to σ. It is possible to calculate b_A as follows: whit $\xi = 0$ at $\sigma \neq 0$ and $T = A_f{}^*$.

$$\alpha_A\left(A_f{}^* - A_s\right) + b_A\sigma = \pi \quad (17)$$

$$\alpha_A\left(A_f - A_s + \Delta Af\right) + b_A\sigma = \pi \quad (18)$$

Recall,

$$\alpha_A = \frac{\pi}{A_f - A_s};\ \sigma = C_A\,\Delta Af \quad (19)$$

Thus,

$$b_A = \frac{-\alpha_A}{C_A} \quad (20)$$

Similarly,

$$b_M = \frac{\alpha_M}{C_M} \quad (21)$$

The effect of increased effect is to shift the characteristic to the right in (Fig. 5) with

$$\xi = \frac{1-\xi_0}{2}\cos[\alpha_M\,(T - M_f) + b_M\sigma] + \frac{1+\xi_0}{2} \quad (22)$$

for $(A \rightarrow M)$ transformation.

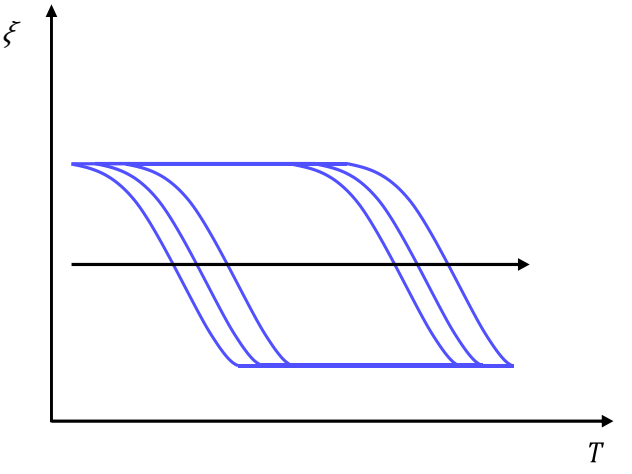

Fig. 5 Shift of ξ-T characteristic to the right with increased stress.

For $(M \rightarrow A)$ transformation, from (16),

$$\left.\begin{aligned} \xi &= \frac{\xi_0}{2}\{1 + \cos\theta\} \\ \theta &= \alpha_A(T - A_s) + b_A\sigma \\ 0 &\le \theta \le \pi \end{aligned}\right\} \quad (23)$$

The range for σ to produce stress-induced martensite can be found to be

$$0 \le \alpha_A(T - A_s) + b_A\sigma \le \pi \quad (24)$$

Thus,

$$0 \le C_A(T - A_s) \quad (25)$$

represents the upper limit for σ.

The lower limit can be found with

$$\alpha_A(T - A_s) + b_A\sigma = \pi \quad (26)$$

$$C_A(T - A_s) + \frac{\pi}{b_A} = \sigma \quad (27)$$

Therefore,

$$C_A(T - A_s) - \frac{\pi}{|b_A|} \le \sigma \quad (28)$$

and thus,

$$C_A(T - A_s) - \frac{\pi}{|b_A|} \le \sigma \le C_A(T - A_s) \quad (29)$$

Holds for the $M \rightarrow A$ transformation.

Similarly,

$$C_M(T - M_f) - \frac{\pi}{|b_M|} \le \sigma \le C_M(T - M_f) \quad (30)$$

The cosine function for ξ allows us to determine the range of stress within which these transformations may take place. With $b_A = \frac{-\alpha_A}{C_A}$ and $b_M = \frac{-\alpha_M}{C_M}$, the range can be shown to be, for $A \to M$,

$$C_M(T - M_f) - \frac{\pi}{|b_M|} \le \sigma \le C_M(T - M_f) \quad (31)$$

and for the reverse transformation $M \to A$,

$$C_A(T - A_s) - \frac{\pi}{|b_A|} \le \sigma \le C_A(T - A_s) \quad (32)$$

These define the ranges in which stress-induced transformations may take place.

Consider

$$C_M(T - M_f) - \frac{\pi}{|b_M|} \le \sigma \quad (33)$$

Then,

$$\sigma = C_M(T - M_f) - \frac{\pi}{|b_M|} \quad (34)$$

represents the lower limit for σ above which a fully austenitic wire will begin to experience the martensitic phase. Let us define this lower limit as $\sigma = \bar{\sigma}_{LIN}$. Thus,

$$\bar{\sigma}_{LIN} = C_M(T - M_f) - \frac{\pi}{|b_M|} \quad (35)$$

and because

$$b_M = \frac{-\alpha_M}{C_M} \quad (36)$$

$$\bar{\sigma}_{LIN} = C_M(T - M_f) - \pi\frac{C_M}{\alpha_M} \quad (37)$$

However, $\alpha_M = \frac{\pi}{M_s - M_f}$, so

$$\bar{\sigma}_{LIN} = C_M(T - M_f) \quad (38)$$

The subscript line also represents the limit of linearity for the stress above, for which the stress-strain relationship will be nonlinear of nonzero martensite.

$$\bar{\varepsilon}_{LIN} = \frac{\bar{\sigma}_{LIN}}{E} \quad (39)$$

2.2 Constitutive modeling of the shape memory effect

The stress state in an SMA component is a function of three primary state variables such as the fraction of martensite, the temperature at which the component is operating, and the strain at which the component is functioning.

Therefore, $\bar{\sigma} = \bar{\sigma}(\bar{\varepsilon}, T, \xi)$. Note that $\bar{\sigma}$ is the Piola-Kirchoff stress, and the $\bar{\varepsilon}$ is the Green strain.

$$\dot{\bar{\sigma}} = \frac{\delta\bar{\sigma}}{\delta\bar{\varepsilon}}\dot{\bar{\varepsilon}} + \frac{\delta\bar{\sigma}}{\delta\bar{T}}\dot{T} + \frac{\delta\bar{\sigma}}{\delta\bar{\xi}}\dot{\bar{\xi}} \quad (40)$$

Integrating with respect to time from the initial conditions $\bar{\varepsilon_0}$, T_0, $\bar{\xi_0}$, we can write a unified constitutive relation.

$$\bar{\sigma} - \overline{\sigma_0} = D(\bar{\varepsilon} - \bar{\varepsilon_0}) + \theta\,(T - T_0) + \Omega(\xi - \xi_0) \quad (41)$$

where D = Young' modulus, θ = thermoelastic tensor, and Ω = transformation tensor. An isothermal condition implies $T = T_0$, $\sigma < C_M(T - M_f)$, $\xi = \xi_0$. Assume zero initial strain, $\bar{\varepsilon_0} = 0$, at $t = 0$, $\overline{\sigma_0} = 0$, $\bar{\xi_0} = 0$, $T = T_0$. Under these conditions, if the component is loaded and unloaded, it is going to be in the linear region in which $\bar{\sigma} = D\bar{\varepsilon}$, and the linear elastic limit is as follows.

$$\bar{\sigma}_{LIN} = C_M(T - M_f) \quad (42)$$

$$\bar{\varepsilon}_{LIN} = \frac{\bar{\sigma}_{LIN}}{D} \quad (43)$$

When $\bar{\sigma} > \overline{\sigma_0}$, the excess stress induces martensite, and the constitutive relation becomes

$$\bar{\sigma} - \overline{\sigma_0} = D(\bar{\varepsilon} - \bar{\varepsilon_0}) + \Omega(\bar{\xi} - \bar{\xi_0}) \quad (44)$$

with $\overline{\sigma_0} = \bar{\sigma}_{LIN}$, $\bar{\varepsilon_0} = \bar{\varepsilon}_{LIN}$, $\bar{\xi}$=0 and

$$\bar{\sigma} - \bar{\sigma}_{LIN} = D\bar{\varepsilon} - D\bar{\varepsilon}_{LIN} + \Omega\,\bar{\xi} \quad (45)$$

Because,

$$\bar{\sigma} = D\bar{\varepsilon} + \Omega\,\bar{\xi} \quad (46)$$

$$\bar{\sigma}_{LIN} = D\bar{\varepsilon}_{LIN} \quad (47)$$

Thus, the governing equation when $\sigma > \sigma_{LIN}$ are

$$\bar{\sigma} = D\bar{\varepsilon} + \Omega\,\bar{\xi} \quad (49)$$

$$\bar{\sigma}_{LIN} = C_M(T - M_f) \quad (50)$$

$$\bar{\varepsilon}_{LIN} = \frac{\bar{\sigma}_{LIN}}{D} \quad (51)$$

$$\xi = \frac{1-\xi_A}{2}\cos[\alpha_M\,(T - M_f) + b_M\sigma] + \frac{1+\xi_A}{2} \quad (52)$$

for the $A \to M$ transformation.

Referring to the determination of Ω, it is possible to notice the changes in the (Fig. 6). First of all, a wire is unloaded when $\xi = 1$. Recall that the reference temperature is less than A_s. After the unloading, the stress reaches zero, but the strain remains at the maximum limit it attained under σ_{LIN}. It is a linear martensitic elastic unloading.

When $\xi = 1$,

$$\bar{\sigma} = 0 = D\bar{\varepsilon}_{LIN} + \Omega\xi \quad (52)$$

$$\bar{\varepsilon}_L = -\frac{\Omega}{D}\,\xi \quad (53)$$

$$\bar{\varepsilon}_{RES} = -\frac{\Omega}{D}\xi = \bar{\varepsilon}_L \quad (54)$$

Thus,

$$\xi = -\bar{\varepsilon}_{RES}\frac{D}{\Omega} = -\bar{\varepsilon}_{RES}\frac{1}{\bar{\varepsilon}_L} = \frac{\bar{\varepsilon}_{RES}}{\bar{\varepsilon}_L} \quad (55)$$

where ξ is the stress-induced martensite.

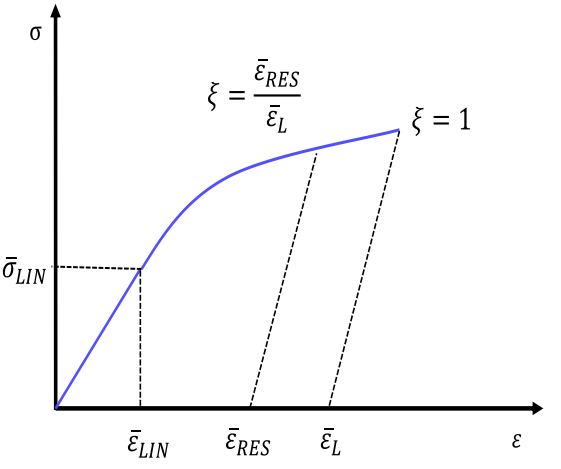

Fig. 6 Stress-strain for unloading a wire.

Typical stress-strain characteristics of shape memory alloys at various temperatures are illustrated in Fig. 7.

2.3 Numerical SMA thermomechanical model

The numerical implementation of a previously described detailed constitutive model represents a significant step in the analysis of SMAs. The use of a UMAT has been decisive in integrating both pseudo-elastic and shape memory effects of SMAs. The distinctive feature of this implementation is the presentation of the proposed 3D finite element model. This

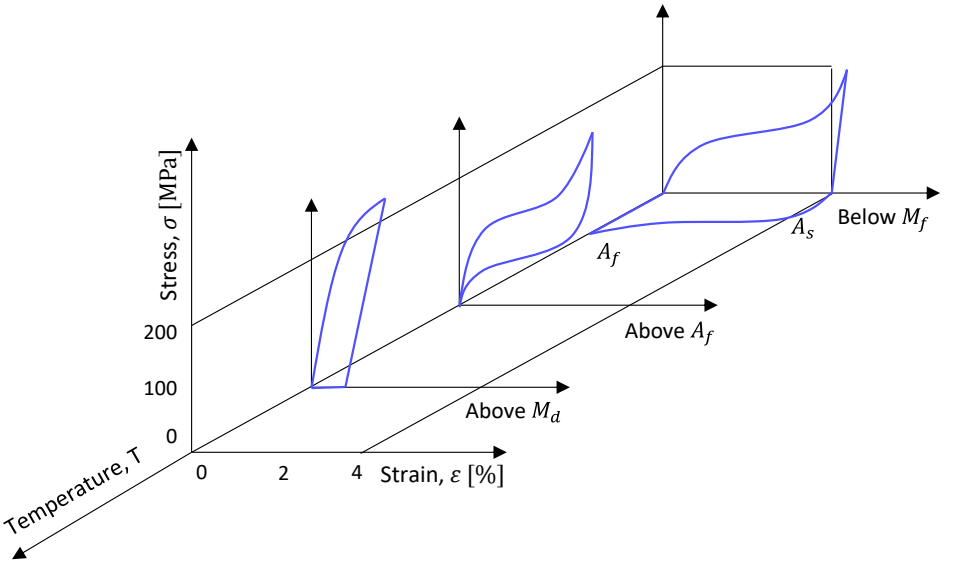

Fig. 7 Variation of stress-strain characteristics of SMA with temperature.

approach leads to greater accuracy in the calculations of thermal and mechanical properties, representing a step forward in the practical application of SMAs. Furthermore, the ability to specifically evaluate the volume fraction contributes to a more detailed performance analysis, leading to improvements in the design and optimization of SMA-based devices. The UMAT emerges as an indispensable tool for addressing such challenges. Indeed, possessing a numerical model capable of accurately replicating real-world phenomena enables swift and precise design. The implemented UMAT concurrently incorporates the principal effects of shape memory alloys, facilitating the design of solutions that necessitate the combined influence of these two elements (Fig. 8).

In the development of the UMAT and the accurate modeling of alloy behaviour, a set of state variables has been introduced to control variations within the material during analysis. This meticulous approach ensures a comprehensive representation of the material's response, contributing to a deeper understanding of its mechanical characteristics. The inclusion of these variables enhances the UMAT's capacity to faithfully capture and predict the intricate mechanical responses of shape memory alloys under diverse loading conditions.

The implemented procedure consists of three main sections: the first dedicated to the calculation and updating of the system stiffness matrix, the second to the stress-strain relationships based on the phase diagram and, finally, the updating of the thermal and total stress matrix (Fig. 9).

3. Numerical results

Once the thermomechanical behaviour of the alloys has been defined and implemented, a numerical validation of the

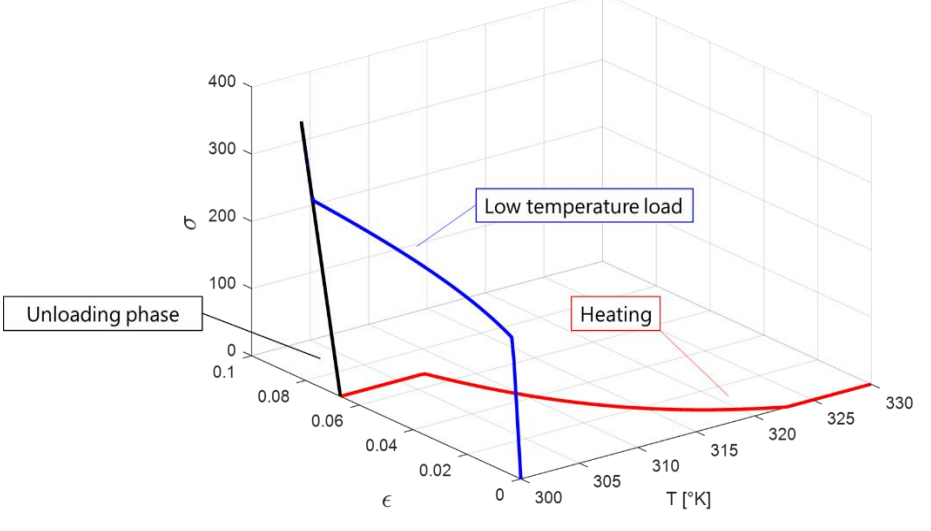

Fig. 8 Pseudoelasticity and shape memory effect.

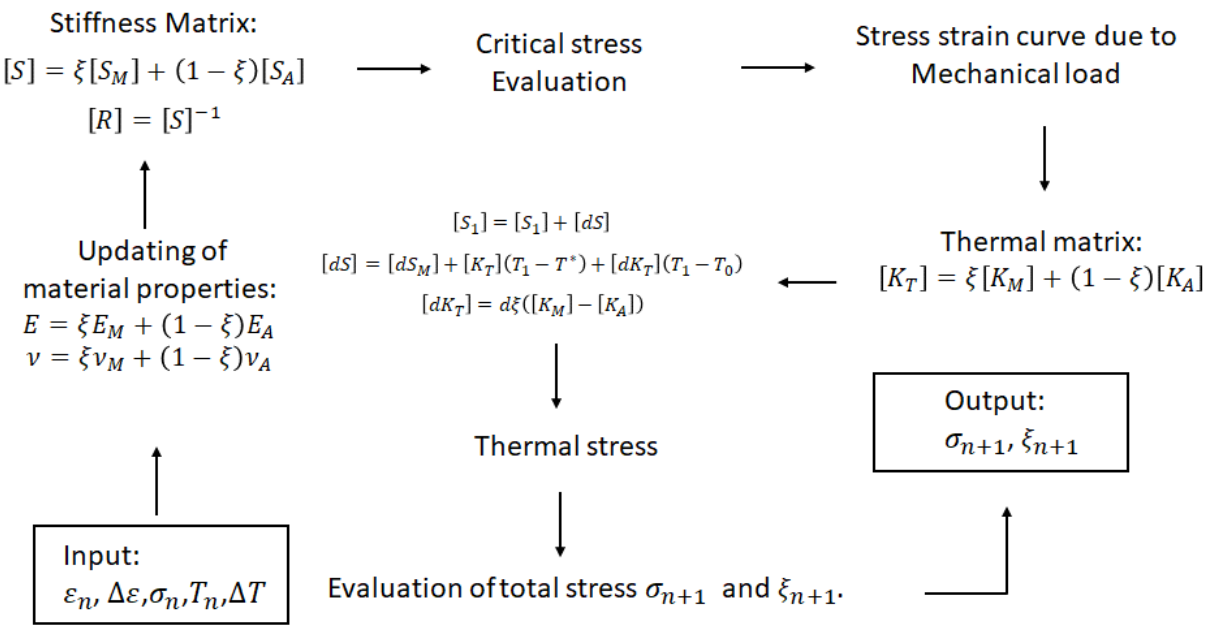

Fig. 9 Workflow UMAT.

UMAT has been conducted to ensure the accuracy it can provide in a numerical environment.

Numerical validation has been performed by comparing the numerical results of an SMA spring operating in phase opposition with two bias springs and the experimental work outlined in Ref. [41]. All geometric parameters and thermomechanical properties of the SMA from the research are reported in the numerical framework. The SMA spring's dimensions include a length of 106 mm, a cold length of 58 mm, and a hot length of 64 mm. During thermal recovery, the SMA spring can ensure a displacement of 6 mm and a force within the range of 90 ± 5 N, achieved at a heating temperature of 110 °C (Fig. 10).

To conduct the experimental test, a SMA spring and an opposing-phase bias spring have been used. The bias spring has a linear stiffness of 0.8 N/mm.

Before analysing the actuation system, a preliminary numerical analysis of the SMA spring has been performed to understand its compression and release characteristics. The SMA spring has been precompressed at a temperature of 25 °C, initially reaching a length of 61 mm. During the free-release phase, it recovered approximately 19 mm of deformation, reaching a force of zero and thus entering its equilibrium phase. Once the SMA spring behaviour has been analysed, it has

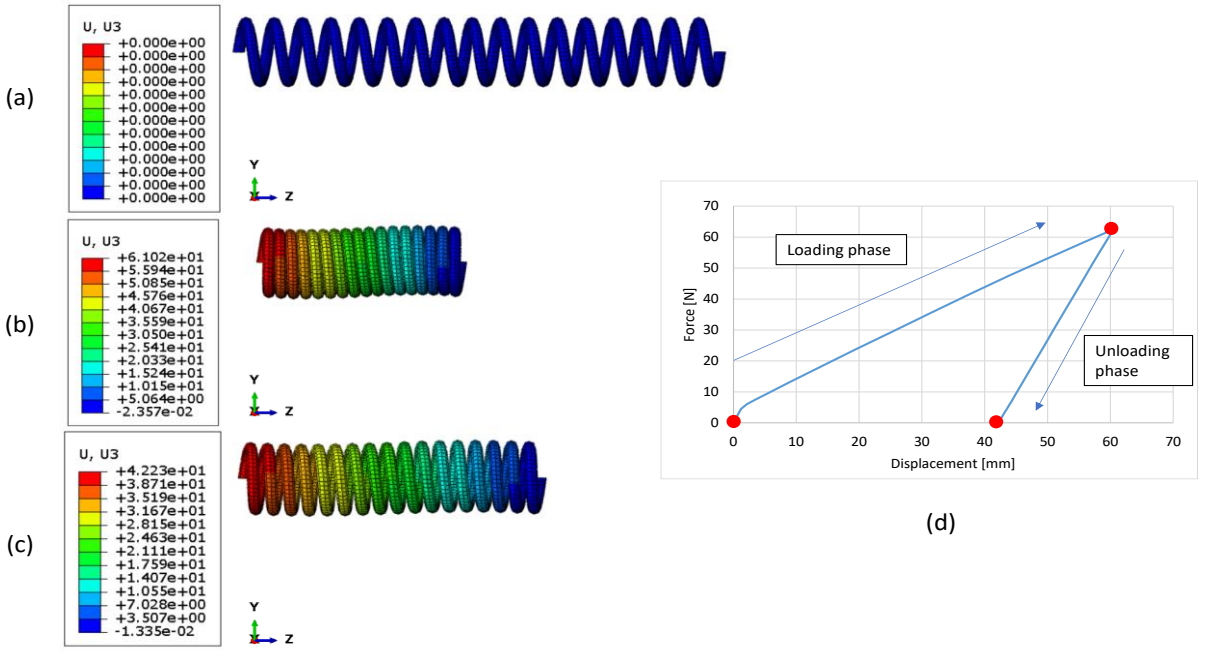

Fig. 10 Numerical results on SMA spring. (a) SMA spring at the beginning of the analysis; (b) displacement at the end of the loading phase; (c) displacement at the end of the unloading phase; (d) Force results of the loading and unloading phases.

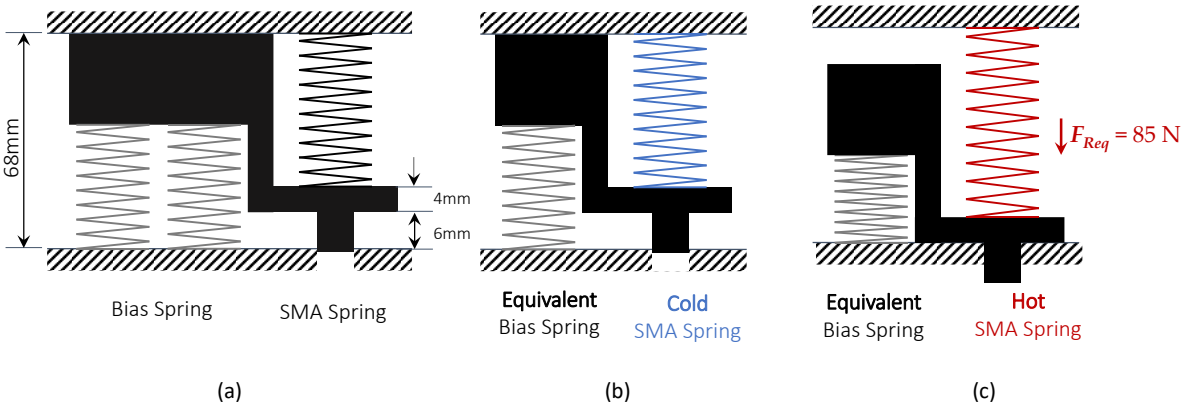

Fig. 11 (a) Operating scheme of actuator; (b) Cold SMA spring compressed; (c) heating of the SMA spring.

been incorporated into the complex system as illustrated in Fig. 11. In accordance with the experimental setup instructions, which specified housing for the cold SMA spring of about 58 mm, the release phase of the spring up to this specific length has been examined. In this context, the spring did not reach a state of zero force but exhibited a force of 25 N and an axial deformation recovery of 13 mm.

According to analytical data, the bias spring must provide a force of 30 N to balance the system, leading it to a new equilibrium phase. Once the system stabilized, the SMA spring has been heated to a temperature of 110 °C, not only ensuring a 6 mm actuator stroke but also generating a force of 87 N, surpassing the required force (Fig. 12).

Emphasizing that the numerically obtained results align entirely with the experimental data, the successful correlation between numerical simulations and experimental findings underscores the reliability and accuracy of the computational model. The results enable the use of the subroutine to design custom-engineered components. This theoretical framework has been effectively employed in the conceptualization and design of a bistable actuator.

SMA actuators exhibit remarkable efficiency in terms of generated forces and low mass. As highlighted in the research conducted by Mohd Jani *et al.*,[42] SMA actuators demonstrate a substantial advantage, boasting 200% more work per volume compared to hydraulic actuators and a 150% increase in power per volume. Generally, compared to other actuators, they exhibit low efficiency due to a reduced actuation frequency and limited controllability. Moreover, continuous application of current is necessary for activation. Additionally, to minimize activation time, heating occurs within very brief intervals using high currents, leading to material degradation.[43-45] Bistable actuators based on SMA materials emerge as particularly efficient solutions compared to other actuator types. The bistable characteristic of SMA actuators allows them to maintain two stable equilibrium positions without the need for a continuous flow of electric current.

The research focuses on the numerical analysis of the designed and patented actuator described in Ref. [46]. Through in-depth simulations, a robust numerical justification is provided for the main characteristics of this actuator. The high efficiency resulting from its bistable configuration makes it particularly interesting in the field of actuators, as it eliminates the need for continuous current flow, as reported in Refs. [34,35]. Moreover, the compact dimensions and rapid activation velocity are critical factors that make it especially suitable for engineering solutions requiring high precision, substantial activation force, and minimal spatial footprint.

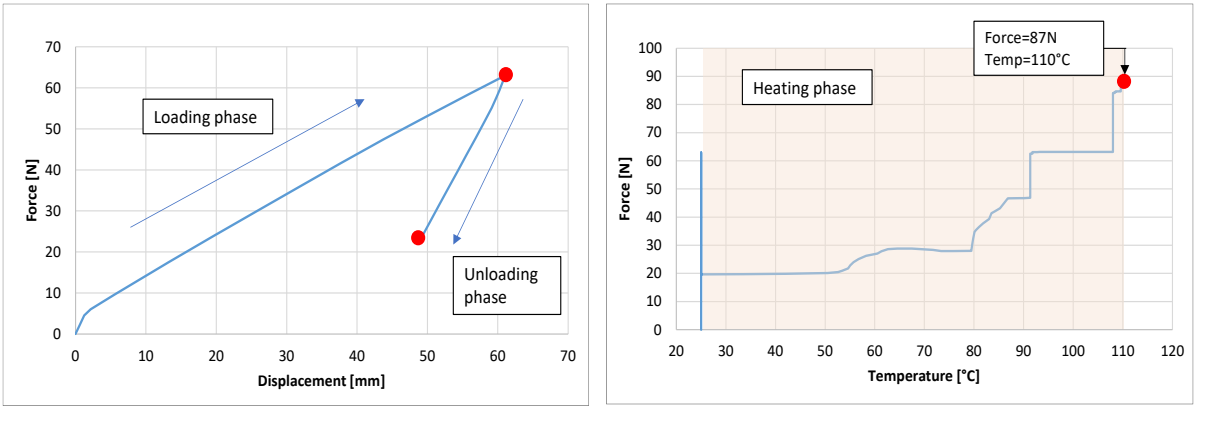

Fig. 12 Numerical results. (a) the loading and the unloading phase of the Cold SMA spring; (b) thermal recovery of the SMA spring.

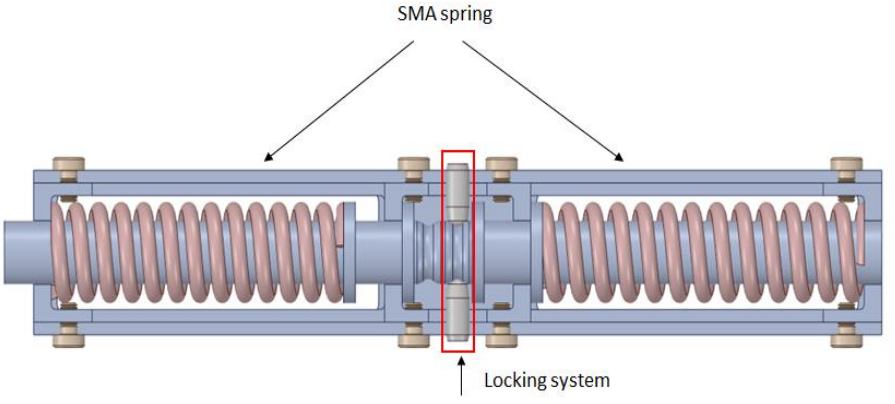

Fig. 13 Bistable actuator.

Indeed, the bistable actuator analyzed in this study can generate a high actuation force while maintaining compact dimensions, especially in comparison to similar actuators.[36,37] The actuator is composed of several elements, including a central body, two SMA springs operating in opposition, two blocking springs, and an outer casing (Fig. 13). Fixed components of the system consist of the external case, facilitating connections to external parts, the locking springs designed with a stiffness of 7 N/mm, and the outer segments of the SMA springs, which are contained within the casing.

The moving component responding to the thrust of the SMA springs is the central body, capable of sliding along the longitudinal direction for a maximum stroke of 5 mm. Once past the initial position, the central body is securely held in the second position by two locking springs that surpass the force exerted by the SMA springs (Fig. 14).

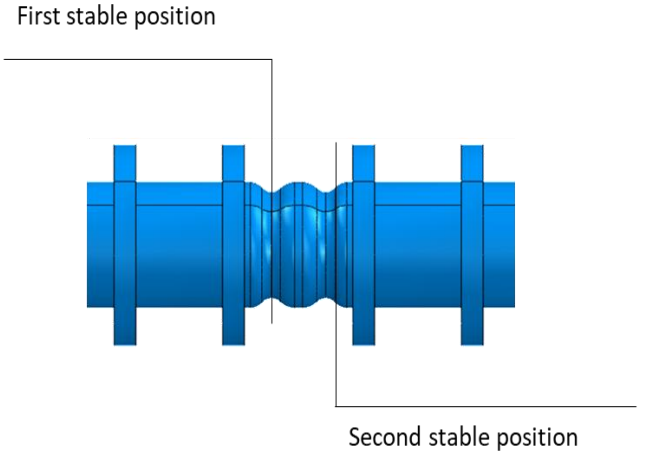

Fig. 14 Bistable actuator positions.

The material used for SMA springs is a nickel and titanium alloy, and its properties (Table.1) have been extrapolated from experimental tests reported in Ref. [41,47].

A preliminary analysis has been necessary to evaluate the mechanical characteristics and force generation of the springs, focusing on the SMA spring at a temperature of 25 °C. The geometric characteristics of the two SMA springs include a length of about 105 mm, a coil number of 17, and a filament diameter of 2.6 mm. A precompression of 55 mm was applied to the bottom part of the spring while the opposite one was clamped. The spring's mechanical behavior is depicted in Fig. 15a; during the loading phase, it reaches a compression load of 55 mm and a force of 68 N.

Table 1. Nickel titanium naval ordnance laboratory (NiTiNOL) thermo-mechanical properties.

	Nitinol		
$\sigma_{scr}\ [MPa]$	15	$\alpha_M\ [1/K]$	2.2×10^{-6}
$\sigma_{fcr}\ [MPa]$	100	$\alpha_A\ [1/K]$	2.2×10^{-6}
$E_M\ [GPa]$	51.87	ε_l	0.05
$E_A\ [GPa]$	115.87	$M_s\ [K]$	338
$C_M\ [MPa/K]$	8	$M_f\ [K]$	303
$C_A\ [MPa/K]$	8	$A_s\ [K]$	328
ν_M	0.33	$A_f\ [K]$	381
ν_A	0.33		

Although the figure clearly shows that the SMA spring does not complete the transformation, it is essential to emphasize that this choice has been deliberate and oriented toward the specific needs of the application in question. The adoption of a partial transformation has been guided by a design aimed at achieving an optimal balance between the desired performance and the unique requirements of the system. In general, failure to fully transform an SMA spring during the loading phase can have a significant impact on overall performance. Variables such as temperature, applied load, and spring design can affect this. The consequences of incomplete transformation are different, including potentially limiting the overall efficiency of the device or system in which the spring is used. In addition, the thermomechanical response could be compromised, possibly affecting the spring's ability to generate the desired force or displacement. In this context, the choice of a partial transformation has been directed by the need to carefully balance these factors, seeking an optimal compromise between the specific needs of the application and the overall performance of the system.

Subsequently, the 55 mm load has been removed, allowing the spring to deform and recover approximately 32% of the initial displacement. After stabilization, a thermal load of

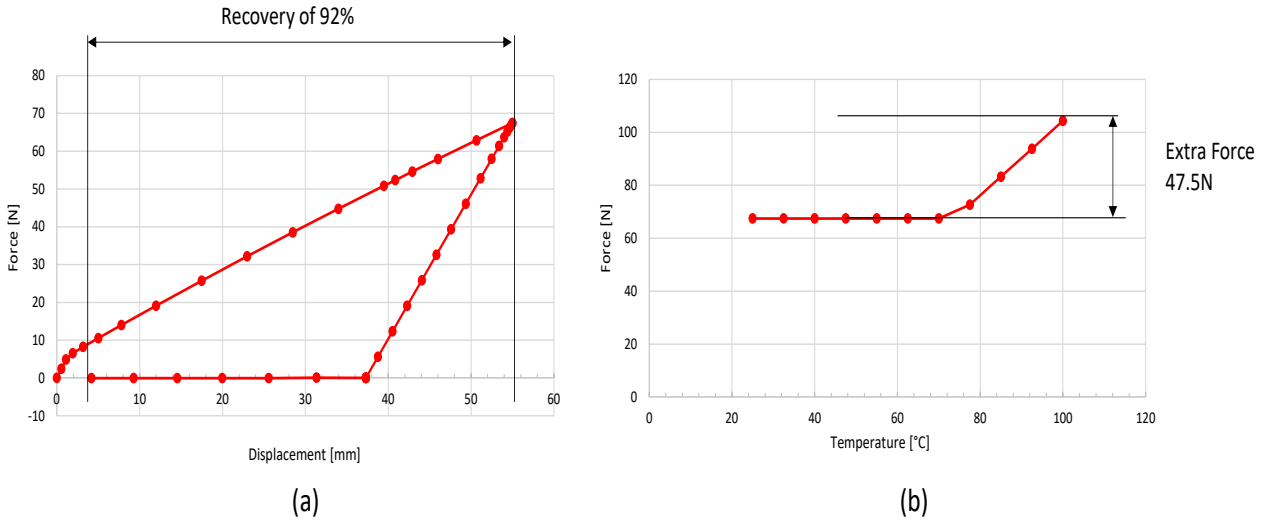

Fig. 15 SMA spring results. (a) Force–displacement graph; (b) Force–temperature graph.

100 °C was applied, resulting in the recovery of 92% of the deformation and the generation of a force of about 115 N (Fig. 15b), showing an extra force of about 47.5 N.

The volumetric martensite fraction is a central aspect in the characterization of the thermomechanical behavior of an SMA spring. In the context of the UMAT, its sensitivity emerges as it allows the entire transformation state of the spring to be uniquely defined. The UMAT, being highly accurate, is able to accurately capture the volumetric changes occurring during the phase transition of martensite in the spring. This detailed response capability allows accurate assessment of volumetric deformations during different stages of the thermomechanical process.

In Fig. 16, the changes in the volume fraction of martensite in the SMA spring (variable SDV7) are depicted across different load steps (spring fully preloaded at 25 °C and spring at 100 °C). As indicated by Fig. 16, the transformation of the SMA spring into martensite is incomplete ($\xi < 1$). This implies the potential for enhancing the spring's efficiency in terms of the specific load by optimizing its geometric features.

A detailed approach involving seven separate numerical steps was used to complete the calibration of the SMA actuator. This division of the entire analysis has been essential to simulate the complete process and ensure a high degree of accuracy in the analysis of all results. The first phase involves the compression of the two SMA springs, followed by the second phase involving the compression of the two conventional springs. The third phase includes the unloading phase, while the fourth provides for the heating of the first SMA spring. Next, the fifth phase features the cooling process, followed by the sixth phase of stabilization. The seventh and final phase focuses on the heating of the second SMA spring. The displacement is driven only by the SMA springs, which move the actuator toward the second equilibrium position Fig. 17a. It should be noted that the actuator does not exhibit any critical stresses. The highest stress value is observed in the central part, adjacent to the side springs, with a value of 20 MPa (Fig. 17b).

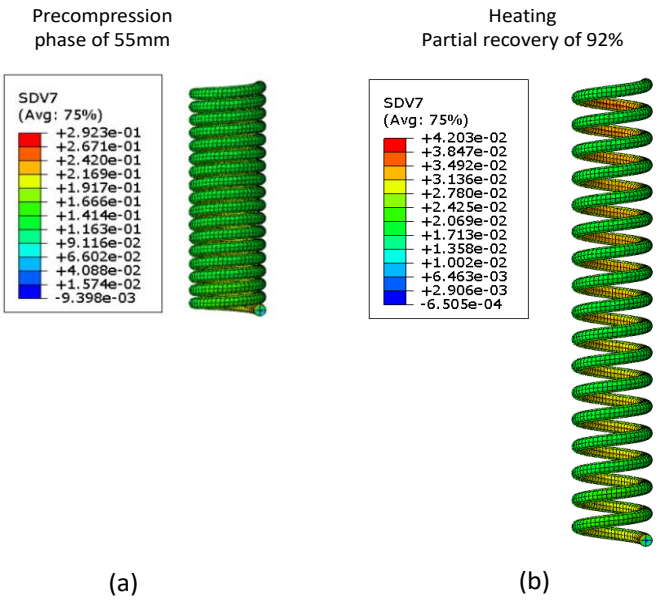

Fig. 16 Volume fraction of martensite. (a) Precompression phase of 55mm; (b) Partial recovery of 92%.

4. Additive configuration and experimental setup

The actuator, meticulously designed and subjected to numerical analysis, has been produced with additive technology and Roboze's Carbon Peek material (Fig. 18). This material has been selected for its great thermal resistance properties; indeed, it is able to withstand temperatures of up to 280 °C for short periods of time. Mechanical and thermal properties are reported in Ref. [48].

Opting to integrate two cutting-edge technologies into a singular project has been a strategic decision that effectively addressed and surpassed the challenges and constraints associated with each technology. While additive technology holds promise, it commonly encounters challenges, particularly concerning temperature considerations. Moreover,

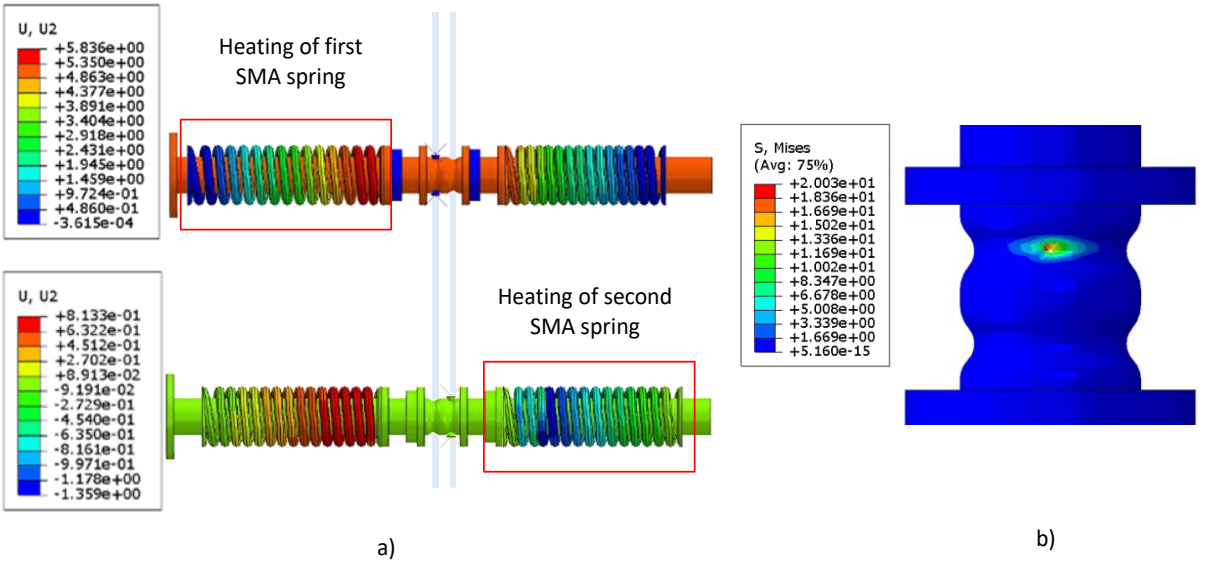

Fig. 17 Numerical Results. (a) Displacement imposed by SMA spring; (b) max Von Mises stress on the actuator.

as a precision-focused mechanism, every component underwent thorough refinement to enhance the performance of all moving parts within the designed system.

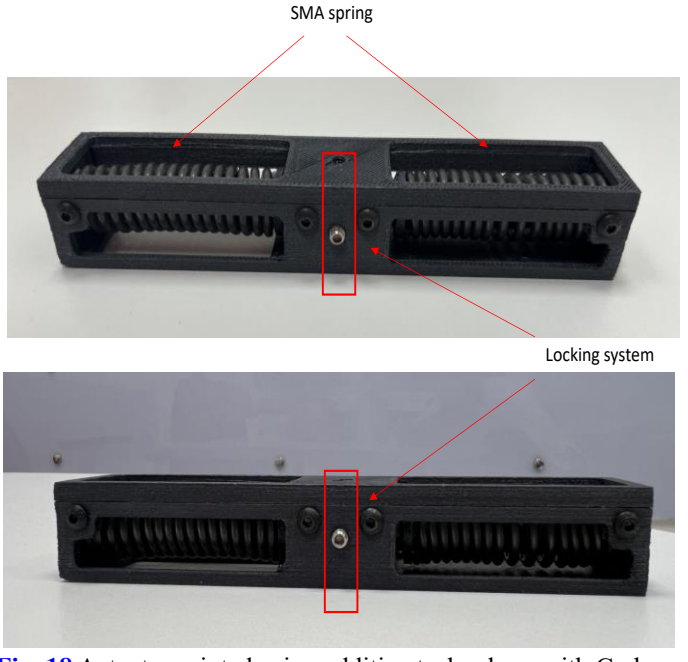

Fig. 18 Actuator printed using additive technology with Carbon Peek material.

The manufactured actuator has been assembled with SMA springs and has been experimentally tested at different current intensities to assess the efficiency in terms of response time (Fig. 19). Numerical analyses have been performed with a temperature of 100 °C for heating the SMA springs, and thus recovering part of the residual deformation. To conduct these tests, one of the two SMA springs has been connected to a bench power supply, allowing the evaluation of response times by appropriately calibrating the current inputs. The results reveal a significant correlation between current intensity and actuator response time. At 10 A, the actuator demonstrates a response time of 40s, while at 20A this value is reduced to 17s. Instead, for a current intensity of 30A, the response time decreases dramatically to only 3s, underlining the actuator's remarkable efficiency and responsiveness to higher electrical loads. A distinctive aspect that emerged from the tests is the actuator's ability to remain stable in the second equilibrium position once the electrical load and, consequently, the thermal load, has been removed. This capability, removing the need to maintain the thermal load, amplifies the actuator's practical applicability and operational effectiveness in various engineering applications.

5. Conclusion

This research presents an in-depth study of the implementation, validation, and practical application of SMA materials for engineering applications. A fundamental theoretical background is the basis of this investigation, enabling the comprehensive implementation of the alloys' thermo-mechanical behavior. The meticulous numerical validation of the UMAT has confirmed its reliability, accurately approximating the behavior of the SMA actuator at a temperature of 110 °C, as confirmed by experimental data from existing literature.

The implications of using the UMAT extend to the design of custom-engineered components, with a particular emphasis on a patented bistable actuator composed of SMA springs and meticulously designed structural elements. This actuator highlights the potential of SMA actuators in terms of efficiency, force generation, and mass reduction. Experimental tests conducted on the actuator, produced using additive technology with Roboze's Carbon Peek material, have revealed significant responsiveness to varying current intensities. The actuator demonstrated remarkable efficiency,

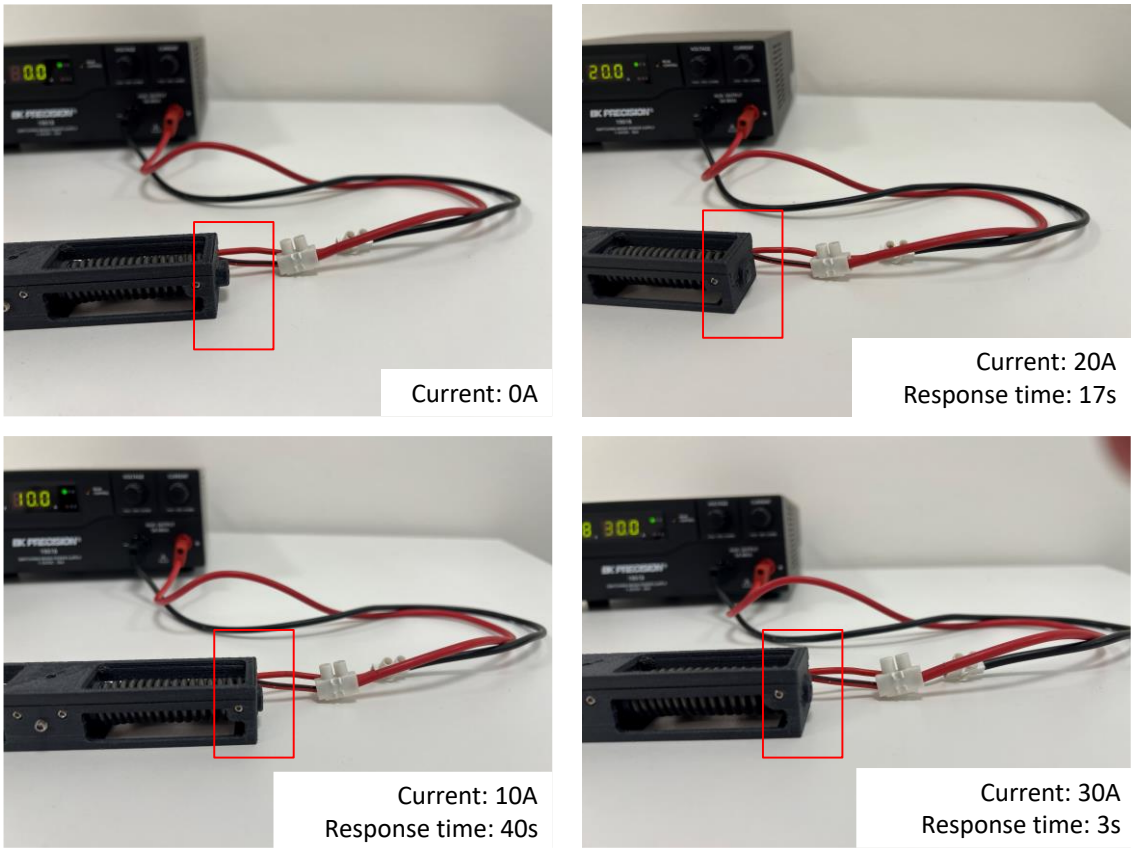

Fig. 19 Experimental test at different currents.

with response times of 40s at 10A, 17s at 20A, and an impressive 3s at 30A. Moreover, the stability of the actuator in the second equilibrium position after the removal of electrical and thermal loads eliminated the need to continuously maintain the thermal load. This research connects the theory of shape memory alloys to practical engineering applications, combining the use of additive technology and advanced materials to address challenges in the fields of temperature and surface finish of additive materials. The integration of these cutting-edge technologies not only improves the performance of actuators, but also expands their applicability in all fields of engineering.

Conflict of Interest

There is no conflict of interest.

Supporting Information

Not applicable.

References

[1] C. Fang, W. Wang, Y. Ji, M. C. H. Yam, Superior low-cycle fatigue performance of iron-based SMA for seismic damping application, *Journal of Constructional Steel Research*, 2021, **184**, 106817, doi: 10.1016/j.jcsr.2021.106817.

[2] C. V. Katsiropoulos, P. Pappas, N. Koutroumanis, A. Kokkinos, C. Galiotis, Improving the damping behavior of fiber-reinforced polymer composites with embedded superelastic shape memory alloys (SMA), *Smart Materials and Structures*, 2020, **29**, 025006, doi: 10.1088/1361-665x/ab6026.

[3] P. Hua, M. Xia, Y. Onuki, Q. Sun, Nanocomposite NiTi shape memory alloy with high strength and fatigue resistance, *Nature Nanotechnology*, 2021, **16**, 409-413, doi: 10.1038/s41565-020-00837-5.

[4] R. S. Ahmed Adnan, M. K. Abbass, D. M. Jomaa, Effect of tin addition on corrosion resistance and microstructure of Cu-based shape memory alloy, *Materials Today: Proceedings*, 2021, **42**, 2119-2124, doi: 10.1016/j.matpr.2020.12.295.

[5] F. Auricchio, E. Boatti, M. Conti, S. Marconi, SMA biomedical applications, *Shape Memory Alloy Engineering*, 2021, 627-658, doi: 10.1016/b978-0-12-819264-1.00019-4.

[6] A. Riccio, A. Sellitto, S. Ameduri, A. Concilio, M. Arena, Shape memory alloys (SMA) for automotive applications and challenges. Shape Memory Alloy Engineering. Amsterdam: Elsevier, 2021.

[7] G. Costanza, M. E. Tata, Shape memory alloys for aerospace, recent developments, and new applications: a short review, *Materials*, 2020, **13**, 1856, doi: 10.3390/ma13081856.

[8] T. Quackenbush, R. McKillip, Selected applications of aeropropulsion actuation and shape control devices using HTSMAs, *Metallurgical and Materials Transactions A*, 2012, **43**, 2870-2881, doi: 10.1007/s11661-011-0998-z.

[9] D. J. Hartl, D. C. Lagoudas, Aerospace applications of shape memory alloys, *Proceedings of the Institution of Mechanical Engineers, Part G: Journal of Aerospace Engineering*, 2007, **221**, 535-552, doi: 10.1243/09544100jaero211.

[10] M. Lalegani Dezaki, M. Bodaghi, A. Serjouei, S. Afazov, A. Zolfagharian, Adaptive reversible composite-based shape memory alloy soft actuators, *Sensors and Actuators A*: *Physical*, 2022, **345**, 113779, doi: 10.1016/j.sna.2022.113779.
[11] S. Akbari, A. H. Sakhaei, S. Panjwani, K. Kowsari, Q. Ge, Shape memory alloy based 3D printed composite actuators with variable stiffness and large reversible deformation, *Sensors and Actuators A*: *Physical*, 2021, **321**, 112598, doi: 10.1016/j.sna.2021.112598.
[12] T. W. Duerig, K. N. Melton, D. W. C. M. Stöckel, Engineering aspects of shape memory alloys, 2013.
[13] L. Xu, T. Baxevanis, D. C. Lagoudas, A three-dimensional constitutive model for the martensitic transformation in polycrystalline shape memory alloys under large deformation, *Smart Materials and Structures*, 2019, **28**, 074004, doi: 10.1088/1361-665x/ab1acb.
[14] Y. You, X. Gu, Y. Zhang, Z. Moumni, G. Anlaş, W. Zhang, Effect of thermomechanical coupling on stress-induced martensitic transformation around the crack tip of edge cracked shape memory alloy, *International Journal of Fracture*, 2019, **216**, 123-133, doi: 10.1007/s10704-019-00346-0.
[15] Z.-H. Gong, J. Zhang, S.-T. Song, C.-L. Wang, Hysteretic behavior and recoverability research on the shape memory effect of SMA bars under cyclic loading, *Construction and Building Materials*, 2023, **387**, 131553, doi: 10.1016/j.conbuildmat.2023.131553.
[16] Y. Doi, T. Ishii, H. Cho, T. Sasaki, Effects of the volume fraction of martensitic-phase during buckling deformation on post-buckling behavior of tape-shaped Ti-Ni shape memory alloy element, *Transactions of the Materials Research Society of Japan*, 2021, **46**, 3-8, doi: 10.14723/tmrsj.46.3.
[17] A. J. D. Debossan, L. L. Vignoli, Improving composite low velocity impact performance using SMA: a multiscale analysis, *Mechanics Research Communications*, 2022, **125**, 103996, doi: 10.1016/j.mechrescom.2022.103996.
[18] X. Gu, Y. Zhang, Y. You, X. Ju, J. Zhu, Z. Moumni, W. Zhang, Evolution of transformation characteristics of shape memory alloys during cyclic loading: transformation temperature hysteresis and residual martensite, *Smart Materials and Structures*, 2020, **29**, 095011, doi: 10.1088/1361-665x/ab9f10.
[19] M. S. Kim, J. K. Heo, H. Rodrigue, H. T. Lee, S. Pané, M. W. Han, S. H. Ahn, Shape memory alloy (SMA) actuators: the role of material, form, and scaling effects, *Advanced Materials*, 2023, **35**, 2208517, doi: 10.1002/adma.202208517.
[20] H. Stroud, D. Hartl, Shape memory alloy torsional actuators: a review of applications, experimental investigations, modeling, and design, *Smart Materials and Structures*, 2020, **29**, 113001, doi: 10.1088/1361-665x/abbb12.
[21] H. Jin, Y. Ouyang, H. Chen, J. Kong, W. Li, S. Zhang, Modeling and motion control of a soft SMA planar actuator, *IEEE/ASME Transactions on Mechatronics*, 2022, **27**, 916-927, doi: 10.1109/TMECH.2021.3074971.
[22] J. Arias Guadalupe, D. Copaci, D. Serrano del Cerro, L. Moreno, D. Blanco, Efficiency analysis of SMA-based actuators: possibilities of configuration according to the application, *Actuators*, 2021, **10**, 63, doi: 10.3390/act10030063.
[23] D. Kumar, J. Daudpoto, B. S. Chowdhry, Challenges for practical applications of shape memory alloy actuators, *Materials Research Express*, 2020, **7**, 073001, doi: 10.1088/2053-1591/aba403.
[24] O. Abdulhameed, A. Al-Ahmari, W. Ameen, S. H. Mian, Additive manufacturing: challenges, trends, and applications, *Advances in Mechanical Engineering*, 2019, **11**, 1687814018822880, doi: 10.1177/1687814018822880.
[25] J. J. Beaman, D. L. Bourell, C. C. Seepersad, D. Kovar, Additive manufacturing review: early past to current practice, *Journal of Manufacturing Science and Engineering*, 2020, **142**, 110812, doi: 10.1115/1.4048193.
[26] I. Gibson, D. Rosen, B. Stucker, M. Khorasani, Design for additive manufacturing, *Additive Manufacturing Technologies*, 2021, 555-607, doi: 10.1007/978-3-030-56127-7_19.
[27] A. Wiberg, J. Persson, J. Ölvander, Design for additive manufacturing–a review of available design methods and software, *Rapid Prototyping Journal*, 2019, **25**, 1080-1094, doi: 10.1108/rpj-10-2018-0262.
[28] V. Acanfora, A. Sellitto, A. Russo, M. Zarrelli, A. Riccio, Experimental investigation on 3D printed lightweight sandwich structures for energy absorption aerospace applications, *Aerospace Science and Technology*, 2023, **137**, 108276, doi: 10.1016/j.ast.2023.108276.
[29] B. Sun, Q. Ma, X. Wang, J. Liu, M. R. M. Rejab, Additive manufacturing in medical applications: a brief review, *IOP Conference Series*: *Materials Science and Engineering*, 2021, **1078**, 012007, doi: 10.1088/1757-899x/1078/1/012007.
[30] J. C. Vasco, Additive manufacturing for the automotive industry, *Additive Manufacturing*, 2021, 505-530, doi: 10.1016/b978-0-12-818411-0.00010-0.
[31] H. Williams, E. Butler-Jones, Additive manufacturing standards for space resource utilization, *Additive Manufacturing*, 2019, **28**, 676-681, doi: 10.1016/j.addma.2019.06.007.
[32] M. Bhuvanesh Kumar, P. Sathiya, Methods and materials for additive manufacturing: a critical review on advancements and challenges, *Thin-Walled Structures*, 2021, **159**, 107228, doi: 10.1016/j.tws.2020.107228.
[33] A. Das, C. A. Chatham, J. J. Fallon, C. E. Zawaski, E. L. Gilmer, C. B. Williams, M. J. Bortner, Current understanding and challenges in high temperature additive manufacturing of engineering thermoplastic polymers, *Additive Manufacturing*, 2020, **34**, 101218, doi: 10.1016/j.addma.2020.101218.
[34] R. Britz, P. Motzki, Analysis and evaluation of bundled SMA actuator wires, *Sensors and Actuators A*: *Physical*, 2022, **333**, 113233, doi: 10.1016/j.sna.2021.113233.
[35] R. Courant, J. Maas, Design and characterization of an efficient multistable push-pull linear actuator using magnetic shape memory alloys, *IEEE Access*, 2024, **12**, 107855-107871, doi: 10.1109/ACCESS.2024.3436809.
[36] A. Nespoli, S. Besseghini, S. Pittaccio, E. Villa, S. Viscuso, The high potential of shape memory alloys in developing miniature mechanical devices: a review on shape memory alloy mini-actuators, *Sensors and Actuators A*: *Physical*, 2010, **158**,

149-160, doi: 10.1016/j.sna.2009.12.020.
[37] K. Hu, K. Rabenorosoa, M. Ouisse, A review of SMA-based actuators for bidirectional rotational motion: application to origami robots, *Frontiers in Robotics and AI*, 2021, **8**, 678486, doi: 10.3389/frobt.2021.678486.
[38] L. C. Brinson, One-dimensional constitutive behavior of shape memory alloys: thermomechanical derivation with non-constant material functions and redefined martensite internal variable, *Journal of Intelligent Material Systems and Structures*, 1993, **4**, 229-242, doi: 10.1177/1045389x9300400213.
[39] K. Tanaka, A thermomechanical sketch of shape memory effect: one-dimensional tensile behavior, 1986.
[40] C. Liang, C. A. Rogers, One-dimensional thermomechanical constitutive relations for shape memory materials, *Journal of Intelligent Material Systems and Structures*, 1990, **1**, 207-234, doi: 10.1177/1045389x9000100205.
[41] A. Riccio, C. Napolitano, A. Sellitto, V. Acanfora, M. Zarrelli, Development of a combined micro-macro mechanics analytical approach to design shape memory alloy spring-based actuators and its experimental validation, *Sensors*, 2021, **21**, 5506, doi: 10.3390/s21165506.
[42] J. Mohd Jani, M. Leary, A. Subic, M. A. Gibson, A review of shape memory alloy research, applications and opportunities, *Materials & Design (1980-2015)*, 2014, **56**, 1078-1113, doi: 10.1016/j.matdes.2013.11.084.
[43] J. Qiu, J. Tani, D. Osanai, Y. Urushiyama, High-speed actuation of shape memory alloy, *Smart Structures and Devices*, 2001, **4235**, 188-197, doi: 10.1117/12.420858.
[44] R. Featherstone, Y. H. Teh, Improving the speed of shape memory alloy actuators by faster electrical heating, Experimental Robotics IX: The 9th International Symposium on Experimental Robotics, Berlin, Heidelberg: Springer Berlin Heidelberg, 2006.
[45] C. S. Loh, H. Yokoi, T. Arai, New shape memory alloy actuator: design and application in the prosthetic hand, 2005 IEEE Engineering in Medicine and Biology 27th Annual Conference. Shanghai, China. IEEE, 2006.
[46] M. Battaglia, A. Sellitto, A. Giamundo, M. Visone, A. Riccio, Advanced material thermomechanical modelling of shape memory alloys applied to automotive design, *Shape Memory and Superelasticity*, 2024, **10**, 297-313, doi: 10.1007/s40830-024-00494-w.
[47] A. Riccio, S. Saputo, M. Zarrelli, A. Sellitto, C. Napolitano, V. Acanfora, Shape memory alloy-based actuator: experimental and modelling, 2021 IEEE 8th International Workshop on Metrology for AeroSpace, Naples, Italy, IEEE, 2021.
[48] V. Acanfora, A. Garofano, M. Battaglia, G. Maisto, A. Riccio, On the effect of printing orientation on the surface roughness of an additive manufactured composite vertical tail, *International Journal of Advanced Manufacturing Technology*, 2024, **130**, 4543-4564, doi: 10.1007/s00170-024-12999-w.